Ceramics-Silikáty 60 (2), 34-40 (2016)
journal webpage: www.ceramics-silikaty.cz
doi: 10.13168/cs.2016.0005

HYSTERESIS AND ELECTRIC MODULUS ANALYSIS OF Y^{3+} DOPED MnNi-Y-TYPE HEXAGONAL FERRITE

[#]MUHAMMAD IRFAN*, ** ASMAT ELAHI**, ABDUL SHAKOOR**

*Institute of Physics, Chinese Academy of Sciences, Beijing, China
**Department of Physics, Bahauddin Zakariya University, Multan, Pakistan

[#]E-mail: muhammadiirrffaann@gmail.com

Submitted October 24, 2016; accepted January 20, 2016

Keywords: Y-type hexagonal ferrite, Nano-structure, Cole-Cole diagram, Hysteresis loop

The magnetic, grain morphology and dielectric properties of synthesized $Sr_2MnNiFe_{12}O_{22} + xY_2O_3$ ($x = 0 - 5$ wt.%) ferrite have been investigated via X-ray diffraction (XRD), scanning electron microscopy (SEM) and dielectric spectroscopy, respectively. The nanostructure governs increase in inter-grain connectivity with substitution. The appearance of broad peaks in imaginary electric modulus plots (M") show the existence of relaxation process in all these samples. The grain boundary contribution is clearly observed from Cole–Cole plots. The preferential site occupancy of Yttrium ions results in rapid increase of coercivity, hysteresis loops also revealed same effect of substitution. The improved value of coercivity is quite beneficial for the perpendicular recording media which is an emerging technology in the recording media.

INTRODUCTION

In the race of new inventions, new materials of technological importance have acquired much more attention due to their direct utility, particularly in the field of material science. Hexagonal ferrites have attracted much attention since their discovery by Philips in the 1950s [1].These materials have large utility in the field of material science. These are important magnetic materials that, find its application in almost 70 - 80 % of the electronic materials such as home appliances, communication equipment and data processing devices [2, 3]. Having a high coercivity and moderate magnetization, hexaferrites are valuable from technological point of view. Sr-hexaferrites have attracted much attention for applications in permanent magnetic motor, magnetic recording media and other fields due to its low cost, relatively high coercivity, corrosion resistance and chemical stability [4-6]. These materials have attracted because of excellence chemical stability, mechanical hardness and relatively strong magnetic properties like high magnetic anisotropy, high coercivity and saturation magnetization [7-8]. The application of hexaferrites in high density magnetic recording media require materials with high control of homogeneity, morphology and magnetic properties resulting from their methods of preparation and heat treatments [9, 10]. In order to obtain ultrafine particles for use in high density magnetic recording media, it is essential to find the best synthesis conditions. The sol-gel, the chemical co-precipitation, hydrothermal synthesis, micro emulsion and reverse micelle [11-17]. In the present work, important modification of morphology, dielectric and magnetic properties of Y-type hexaferrites is achieved by doping with a relatively small amount of Y_2O_3. The modification of the above-mentioned properties is suitable for their applications in various electrical devices employed for industrial and military applications. The sol-gel auto-combustion technique has been used to synthesize homogeneous nano-crystallites of hexagonal ferrites because of the simplicity of this technique with respect to both composition and morphology. The chief focus of the present investigation is to prepare a material which is suitable for perpendicular recording media due to improved values of coercivity.

EXPERIMENTAL

Sample preparation

$Sr_2Ni\,MnFe_{12}O_{22} + xY_2O_3$ ($x = 0, 1, 2, 3, 4, 5$ wt. %), were prepared by Sol-Gel auto-combustion technique. The stoichiometric amounts of $Sr(NO_3)_2$, $N_iCl_2\cdot 6H_2O$, $Fe(NO_3)_2\cdot 9H_2O$, $MnCl_2\cdot 3H_2O$ and Y_2O_3 were used. These chemicals were of reagent grade. Since Y_2O_3 was not soluble in deionized water so a measured quantity of Y_2O_3 was dissolved in Nitric acid (HNO_3) and heated up to 200°C which turned into Yttrium nitrate, a soluble salt in water. Using stoichiometric calculations required values of salts were used to make solution in ml of deionized water followed by stirring for 15 min. Citric acid was used as a chelating agent. Ammonia solution was dropped into the solution until the solution was neutral (pH-7). Then the solution became homogeneous stable sol, stirring continued at temperature 80°C, till the Gel was formed. The obtained gel was ignited at 120°C in an open container and was burnt in a self-propagating combustion manner. During auto-combustion, the burning gel expanded rapidly in volume and grew as a dendritic structure. Finally fluffy black powder was obtained. Each sample was ground using mortar and pestel to obtain a homogeneous powder. The powder was then sintered at 1000°C for five hours. The samples were furnace cooled to obtain the equilibrium position of the cations. The sintered powder was then pressed into pellets at a pressure of (~ 30 kPa) using Paul-Otto Weber hydraulic press. Polyvinyl alcohol was used as a binder for making pellets. To evaporate the binder the pellets were kept in a furnace at 300°C for one hour.

Characterization

The structure morphology was identified using SEM instrument, model JEOL JSM-6480. Dielectric properties of the samples were measured using LCR meter (MODEL 8101 INSTEK) in the frequency range 20Hz-1MHz at room temperature. The vibrating sample magnetometer (VSM) Lake Shore (7400, USA), was used to measure M–H loops at room temperature.

RESULTS AND DISCUSSION

X-ray diffraction analysis

Figure 1 shows the X-ray diffractograms of Yttrium doped $Sr_2MnNiFe_{12}O_{22}$ ferrites scanned in the selected 2θ range of 70 – 75 along with complete XRD patterns. The detailed structural information has already been reported in our earlier work [18]. The result was found that Y^{3+} ions could not enter into the lattice of the hexagonal structure but segregate at the grain boundaries and restrain the movement of grain boundaries. The (1 1 30) peak of $Sr_2MnNiFe_{12}O_{22} + xY_2O_3$ hexaferrites shifts slightly towards the lower angle as the doping level increases. This behavior of shifting peak is attributed that the Y^{+3} (r_o (0.89 nm)) ions suppress the grain growth by limiting grain-boundary mobility and hence unit cell squeezes [19].

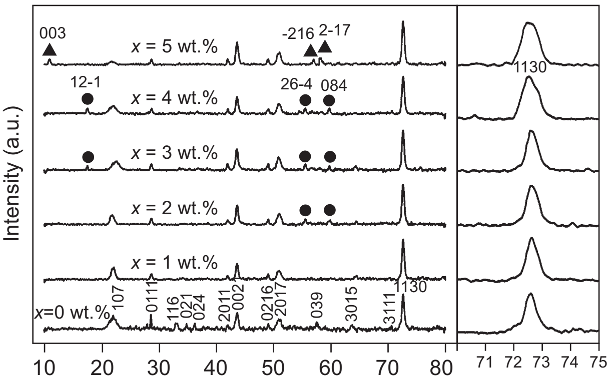

Figure 1. XRD patterns in a 2θ range of 70-75 of the (1 1 30) peak for Y_2O_3 substituted $Sr_2MnNiFe_{12}O_{22}$ hexaferrites.

Surface morphology

The morphology and the particle size of the samples were determined by scanning electron microscopy (SEM). The SEM images Figures 2a-c reveal the effect of different doping level of Y_2O_3 on the microstructure and grain size of Y-type ferrites. The surface morphology shows that as doping increases the grains also become less clearly hexagonal – they become more rounded on the edges, more, irregular shaped, and are no longer such clear hexagonal plates. The diameter of the hexagonal grains seems to be decrease as the doping level increased. The average grain size of the samples was estimated to be in the range of 142.47 to 57.85 nm. This result suggests that Y_2O_3 substitutions did not encourage the grain growth in the Y-type ferrites.

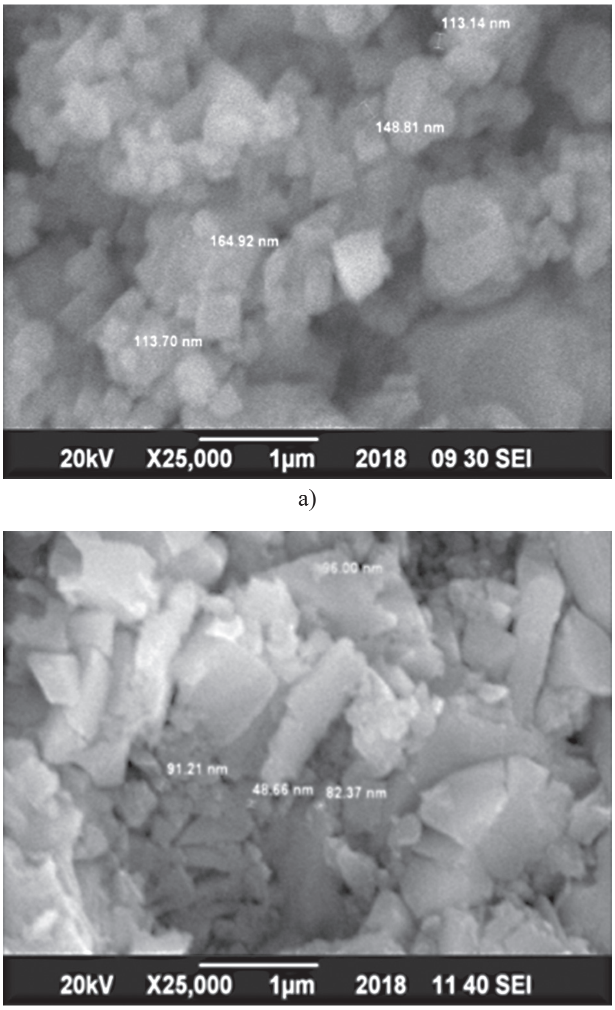

a)

b)

Figure 2. SEM images of Y_2O_3 substituted $Sr_2MnNiFe_{12}O_{22}$ hexaferrites. *(Continue on next page)*

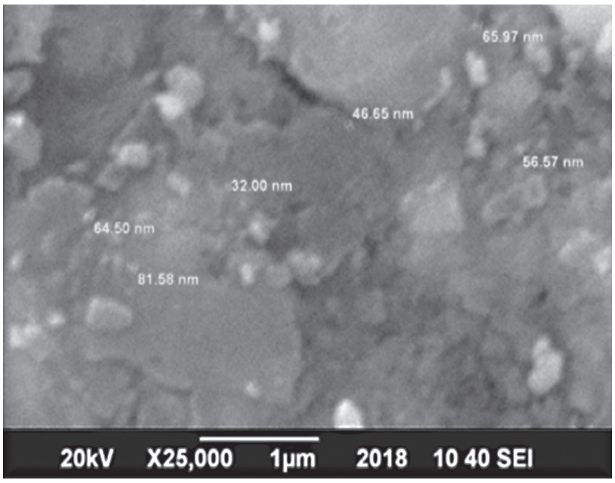

c)

Figure 2. SEM images of Y_2O_3 substituted $Sr_2MnNiFe_{12}O_{22}$ hexaferrites.

Mobility analysis

Drift mobility of all the samples were calculated using the relation

$$\mu_d = \frac{1}{ne\rho} \tag{1}$$

where e is the charge of electron, ρ is resistivity and n is the concentration of charge carrier and can be calculated from the well-known equation;

$$n = \frac{N_A \, d_b \, P_{Fe}}{M} \tag{2}$$

where N_A is the Avogadro's number, d_b is the measured bulk density of sample, P_{Fe} is the number of iron atoms in the chemical formula of the ferrites and M is the molecular weight of the samples. The drift mobility is related to the temperature by following relation

$$\mu_d = \mu_0 \exp\left(\frac{E_\mu}{k_B T}\right) \tag{3}$$

where μ_o is pre-exponential constant, k_B is Boltzmann constant and $E\mu$ is the activation energy for mobility of ions.

In the case of low-mobility semiconductors like ferrites, the activation energy is associated with the charge carrier mobility rather than with charge carrier concentration. The charge carriers are considered as localized at the vacant sites and the conduction arise from charge transfer between the octahedral cations by hopping of localized d-electrons. Drift mobility of the doped samples decreases from 2.20×10^{-8} to 4.02×10^{-12} $cm^2 \cdot V^{-1} \cdot s^{-1} \cdot K^{-1}$ by substitution of Yttrium content. Figure 3 shows the Arrhenius plot and the energy required for the hopping process of electrons for each sample has been calculated and is listed in Table 1.

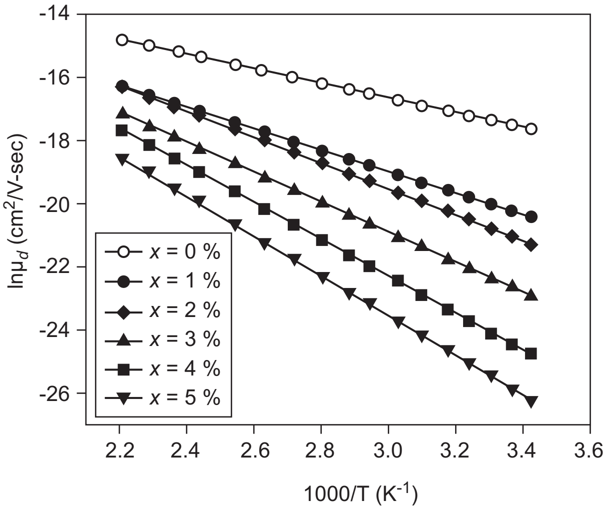

Figure 3. Arrhenius plot for mobility of Y_2O_3 substituted $Sr_2MnNiFe_{12}O_{22}$ hexaferrites.

Complex modulus analysis

The complex modulus formalism is a very important and convenient tool to determine, analyze and interpret the dynamical aspects of electrical transport process in the material, such as the parameters (carrier/ion hopping rate, conductivity relaxation time, etc.) with the smallest capacitance occurring in a dielectric system. As it turns out the effect of conductivity can be highly suppressed when the data are presented in the modulus representation. The electric modulus approach began when the reciprocal complex permittivity was discussed as an electrical analogue to the mechanical shear modulus [20]. The electrical modulus can be written

Table 1. Squarness ratio, magnetic moment, relaxation time, grain size, mobility and activation energy of the studied samples.

Parameters	x = 0 (wt. %)	x = 1 (wt. %) (wt. %)	x = 2 (wt. %)	x = 3 (wt. %)	x = 4 (wt. %)	x = 5 (wt. %)
Mr/Ms	0.40	0.46	0.52	0.57	0.60	0.59
n_B (μB)	11.78	10.12	8.88	6.80	5.55	4.00
τ (μs)	2.56	2.69	2.94	3.05	3.26	3.96
$G{\cdot}S$ (nm)	142.47	–	79.56	–	–	57.85
μ_d (cm^2·V-s-K)	2.20×10^{-8}	1.36×10^{-9}	5.64×10^{-10}	1.09×10^{-10}	1.75×10^{-11}	4.02×10^{-12}
$E\mu$ (eV)	0.19	0.29	0.35	0.40	0.50	0.54

in term of both resistive (real) and reactive (imaginary) components as given below

$$M = \frac{1}{\varepsilon^*} = \frac{1}{\varepsilon' - j\varepsilon''} = M' - jM'' \qquad (4)$$

The variation of real part of electric modulus (M') as a function of frequency is shown in Figure 4. The value of M' is very low in the low frequency region. As frequency increases the value of M' increases and reaches a maximum constant value of $M_\infty = 1/\varepsilon_\infty$ at higher frequencies for all samples. These observations may possibly be related to a lack of restoring force governing the mobility of charge carriers under the action of an induced electric field. These features indicate that the electrode polarization makes a negligible contribution in the material [21].

The frequency dependence of the imaginary part of the electric modulus (M'') exhibits a maximum in Figure 4 (inset). It may be noted from Figure 4 (inset) that the position of the peak shifts to lower frequencies as the doping content is increased. This pattern provides wider information relating charge transport processes such as mechanism of electrical transport, conductivity relaxation, and ion dynamics as a function of frequency. The frequency region below the peak maximum determines the range in which charge carriers are mobile over long distances. At the frequency above peak maximum (high-frequency), the carriers are confined to potential wells, being mobile over short distances. Their region where the peak occurs is indicative of the transition from long-range to short-range mobility with increase in frequency. Further, the appearance of peak in the modulus spectrum provides a clear indication of conductivity relaxation [22]. The condition for observing maxima in (M'') of a material is [23].

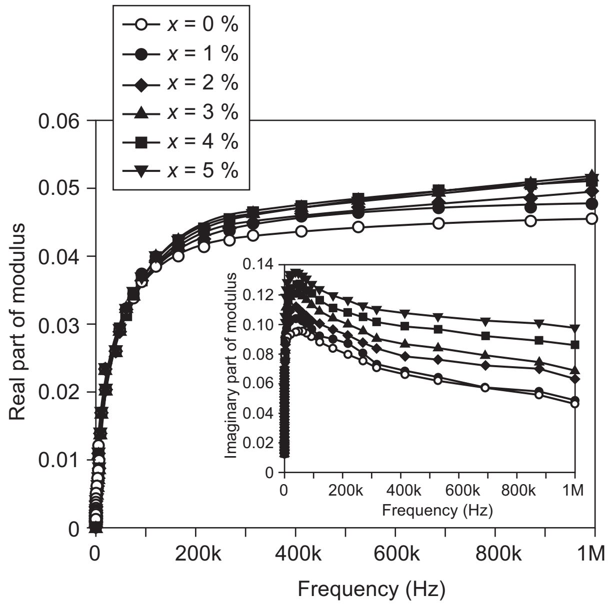

Figure 4. Variation in real part of electric modulus (M') with frequency of Y_2O_3 substituted $Sr_2MnNiFe_{12}O_{22}$ hexaferrites, (inset) showing Variation in imaginary part of electric modulus (M'') with frequency of Y_2O_3 substituted $Sr_2MnNiFe_{12}O_{22}$ hexaferrites.

$$\omega \cdot \tau = 1 \qquad (5)$$

where $\omega = 2\pi f_{max}$ and τ is relaxation time.

Now, the relaxation time is related to jumping probability per unit time P by relation

$$\tau = ½ \cdot P \text{ or } f_{max} \cdot \alpha \cdot P \qquad (6)$$

The value of the relaxation time is given in the Table 1 which indicating the increasing trend with doping content.

Cole–Cole plots

To separate the grain and grain boundary contributions, complex impedance plane plots (Cole–Cole plots) have been investigated. The nano crystalline samples are characterized by small grain size and large number of grain boundaries. The electrical modulus (M) was used, in order to study the frequency dependences of the interfacial polarization effect, which generates electric charge accumulation around the ceramic particles by displacing relaxation peaks. The Maxwell–Wagner model provides to assess the behavior of complex conductivity in heterogeneous systems having two or more phases [24, 25].

In a heterogeneous system, if the region of grain boundary occupies a large volume, the graph of the modulus ($M^* = 1/\varepsilon^*$) M'' versus M' provides better information about the semi circles. It suggests that there is a probable relationship between the behavior of grain boundary and the appearance of the peaks of M″ as a function of frequency. In the second case, if the region of continuity of the grain boundary occupies a small volume, the spectrum of impedance (Z'' versus Z') provides better visualization of the semi circles in the plane. Since there is a probable relationship between the behavior of grain boundary and the appearance of the peaks in M'' as a function of frequency, former case is in great agreement with our present experimental results.

The complex impedance (Cole–Cole) plots using M' and M'' as two variants are plotted in Figure 5. A semi-circle was obtained for all the samples. It was observed from these plots that the major contribution in the conduction is due to grain boundary density. At lower frequency i.e. left side of the semi-circle is a result of grain resistance [26], while the intermediate frequencies represent grain boundary contribution [27]. Taking into account the higher frequency region, extreme right side represents the whole resistance of both grain and grain boundaries [26].

Addition of Y_2O_3 suppresses the grain growth and hence the grain boundaries density increases which in turn leads to a remarkable rise of grain boundary resistance.

Therefore, the conduction mechanism, observed in complex impedance measurement, is well in agreement with the AC conductivity phenomenon, reported earlier. However, as compared to the grain contribution, only grain boundary contribution is clearly observed from Cole–Cole plots. Moreover the resistance of the grain boundary increases with increasing Y_2O_3 contents. The high resistance of the grain boundary contributes in the resistivity and dielectric properties.

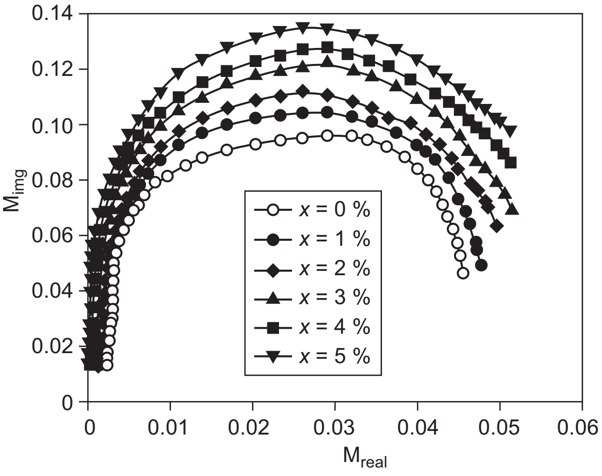

Figure 5. Cole-Cole plot of Y_2O_3 substituted $Sr_2MnNiFe_{12}O_{22}$ hexaferrites at room temperature.

Magnetic hysteresis studies

The saturation magnetization (*Ms*), remanent magnetization (*Mr*), magnetic moment (n_B), and coercivity (*Hc*) of the prepared samples were measured by means of VSM at room temperature. The magnetic pattern of the undoped $Sr_2MnNiFe_{12}O_{22}$ and doped $Sr_2MnNiFe_{12}O_{22}$ + $+ xY_2O_3$ samples for ($x = 0$ - 5 wt. %) is shown in Figure 6. Hysteresis loop in Figure 6 indicate that all the samples exhibit steep rise in magnetization at low applied field followed by a slow variation at high field. The large slope of hysteresis curve is obtained of doped sample at $x = 5$ wt. % at high field indicates unsaturated state. The effect of rare earth element Y^{3+} substitution on the magnetic properties of the material is in general a positive one.

The variation in coercivity with Y^{3+} concentration is shown in Figure 7. This plot indicated that the coercivity increased with the increase in Y^{3+} concentration. This behavior could be explained on the basis of particle size. The particle size estimated from SEM images as given in Table.1 showed that it decreases with increase in Y^{3+} concentration. This decrease in particle size resulted in the increase in coercivity. In the present experimental findings the investigated samples which are Y-type hexaferrites can be used in PRM due to high value of coercivity for $x > 2$ wt. % which is comparable to the those of M-type and W-type hard magnetic materials. Materials are consider to be hard magnets, If $Hc > Mr/2$ and if $Hc < Mr/2$, then the materials are semi-hard magnets [28, 29].

The saturation magnetization decreases with the substitution of Y^{3+} ions as shown in Figure 7. According to Thongmee et al. [30], large size dopant ions go to octahedral sites while small size ions go to tetrahedral sites. If '*Ms'* decreases as in present case, dopant went into spin up sites. The deep observation of the spinel block of Y-type ferrite recalls the fact that super exchange interaction is accountable for magnetic ordering between octahedral $3a_{v1}$ and tetrahedral $6c_{1v}$ sites of the spinel block [31]. In the present investigated samples, the substitution of rare earth ion (Y^{3+} magnetic moment = 0 μ_B) [32] is mainly responsible for diluting magnetic interactions. Y^{3+} had strong preference to $3a_{v1}$ octahedral site, consequently, reducing the super exchange interaction between $3a_{v1}$ and $6c_{1v}$ sites. In this way we can conclude that increasing concentration

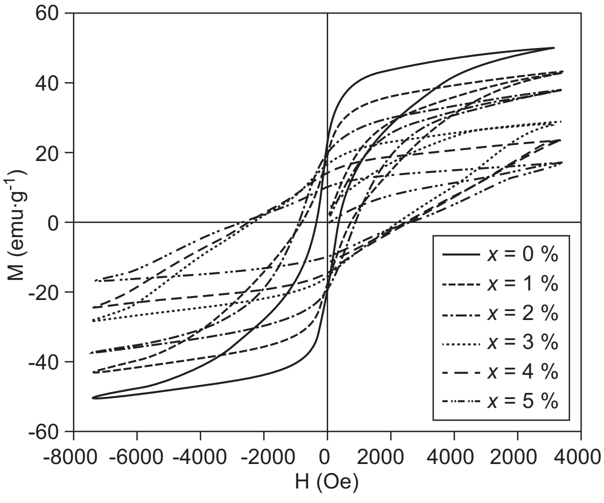

Figure 6. VSM analysis of Y_2O_3 substituted $Sr_2MnNiFe_{12}O_{22}$ hexaferrites at room temperature.

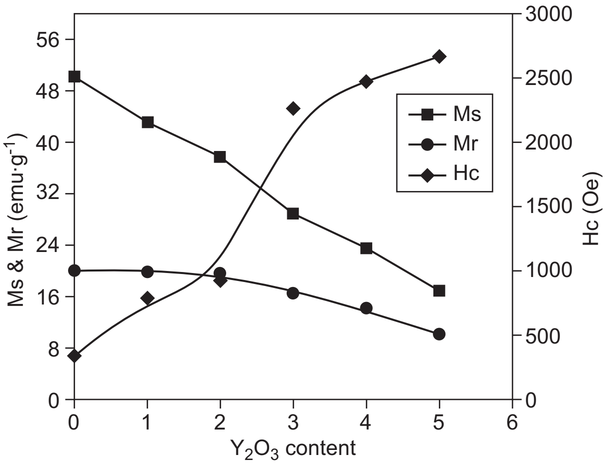

Figure 7. Variation in *Ms*, *Mr* and *Hc* of Y_2O_3 substituted $Sr_2MnNiFe_{12}O_{22}$ hexaferrites.

of Y, the magnetization (M_3a_{v1}) of $3a_{v1}$-sites decreased while that of $6c_{1v}$ site M_6c_{1v} remained constant. As net magnetization is equal toM_3a_{v1}- M_6c_{1v}, so it was found to decrease.

Inverse relation of saturation magnetization and coercivity can be absorbed through browns relation [33] $Hc = K_1/\mu_o Ms$ where K_1 is magneto-crystalline anisotropy, μ_o is vacuum susceptibility, *Ms* is saturation magnetization and *Hc* is coercivity. Our present experimental results of *Ms* and *Hc* are quite satisfactory with this relation, i.e. *Ms* decreases and coercivity increases with increasing substitution level as shown in Figure 7. Similar behavior is reported by many researchers [34, 35]. Figure 7 indicated that the retentivity followed the saturation magnetization i.e. the remanence decreases with doping content. The presences of secondary phases are responsible for the decrease in remanence [36].

The magnetic moment (n_B) is calculated using the following formula:

$$n_B = \frac{M\,Ms}{5585} \tag{7}$$

The values of magnetic moment are listed in Table 1. The values of magnetic moment vary from 11.78 to 4.00 (emu·g^{-1}), which is comparable to already reported values of (n_B) for Y-type hexaferrites [31] within the margin of experimental uncertainty. In present experimental findings behavior of magnetic moment is consistent with the saturation magnetization as both decreases with increasing Y_2O_3 contents. The decrease in magnetic moment can be interpreted as due to the existence of spin canting, promoting the reduction of magnetic moment interactions [37].

Table 1 showed Squarness ratio (*Mr*/*Ms*) for studied samples (ranging 0.40 - 0.60). The ratio is well below the typical value of 1, assigned to single domain isolated ferromagnetic particles. However, the small values of *Mr/Ms* are due to the existence of multi-domain (*MD*) particles in all the samples [38]. This deviation of Squarness ratio from typical single domain value may be attributed to the interaction amongst the grains since they are affected by the grain size distribution in material [39].

CONCLUSION

The variation of magnetic properties of Y^{3+} doped strontium hexaferrites $Sr_2MnNiFe_{12}O_{22}$ have been presented. Yttrium doping suppressed the grain growth and decreased the grain size. Cole-Cole plot showed a single semicircle, indicating the capacitive and resistive properties of the materials; due to contribution of grain boundaries in the studied samples The novel Y-doped Y-type ferrites exhibit excellent static magnetic properties such as low saturation magnetization and high coercivity. It is concluded that two effects contribute to the significant increase of coercivity. One is the increase in the crystalline anisotropy field (intrinsic effect) attributed to the doping of Y content. The other is the decrease in the particle size (extrinsic effect) produced from Y doping restrains the grain growth of hexaferrites particles. The increased anisotropy and reduction of particle size are beneficial for many applications, such as improving signal noise ratio and stability of recording devices**.**

REFERENCES

1. J. Smit, H.P.J. Wijn, Ferrites, Philip's Technical Library, New York, 1959
2. Jotania R.B., Khomane R.B., Chauhan C.C., Menon S.K., Kulkarni B.D. (2008): Synthesis and magnetic properties of barium–calcium hexaferrite particles prepared by sol–gel and microemulsion techniques. *Journal of Magnetism and Magnetic* Materials, *320*(6), 1095-1101. doi:10.1016/j.jmmm.2007.10.032
3. Özgür Ü., Alivov Y., Morkoç H. (2009): Microwave ferrites, part 1: fundamental properties. *Journal of Materials Science: Materials in Electronics*, *20*(9), 789-834. 10.1007/s10854-009-9923-2
4. Garcıa-Cerda L.A., Rodrıguez-Fernandez O.S., Resendiz-Hernandez P.J. (2004) Study of $SrFe_{12}O_{19}$ synthesized by the sol–gel method, *Journal of alloys and compounds*, *369*(1), 182-184. doi:10.1016/j.jallcom.2003.09.099
5. Coey J.M.D. (2002): Permanent magnet applications. *Journal of Magnetism and Magnetic Materials*, *248*(3), 441-456. doi:10.1016/S0304-8853(02)00335-9
6. Singh C., Bindra Narang S., Hudiara I.S., Bai Y., Marina K. (2009): Hysteresis analysis of Co–Ti substitu doi:10.1016/j.matlet.2009.06.002 ted M-type Ba–Sr hexagonal ferrite. *Materials Letters*, *63*(22), 1921-1924.
7. Campbell, P. (1994). *Permanent magnet materials and their application*. Cambridge University Press, Cambridge.
8. Sharrock M.P., Josephson L. (1986): Independent magnetic switching units in cobalt-doped iron oxide particles. *Magnetics, IEEE Transactions on*, *22*(5), 723-725. doi: 10.1109/TMAG.1986.1064545
9. Kryder M.H. (1990): Advances in magneto-optic recording technology. *Journal of Magnetism and Magnetic Materials*, *83*(1), 1-5. doi:10.1016/0304-8853(90)90410-R
10. Ali I., Islam M.U., Ashiq M.N., Iqbal M.A., Karamat N., Awan M.S., Naseem S. (2014): Role of Tb–Mn substitution on the magnetic properties of Y-type hexaferrites. *Journal of Alloys and Compounds*, *599*, 131-138. doi:10.1016/j.jallcom.2014.02.079
11. Irfan M.,Usman M., Elahi a., Khan U., Khan T., Javed K., Ali S.S., Shakoor A. (2015): Influence of Nd^{3+} substitution on physical, electrical and dielectric properties of $Ba_2Zn_2Fe_{12}O_{22}$ hexagonal ferrites prepared by sol–gel auto combustion method. *Journal of Materials Science: Materials in Electronics*. doi: 10.1007/s10854-015-4202-x
12. Zhong W., Ding W., Zhang N., Hong J., Yan, Q., Du Y. (1997): Key step in synthesis of ultrafine $BaFe_{12}O_{19}$ by sol-gel technique. *Journal of Magnetism and Magnetic Materials*, *168*(1), 196-202. doi:10.1016/S0304-8853(96)00664-6

13. Jacobo S.E., Domingo-Pascual C., Rodriguez-Clemente R., Blesa M.A. (1997): Synthesis of ultrafine particles of barium ferrite by chemical coprecipitation. *Journal of materials science*, *32*(4), 1025-1028. doi: 10.1023/A:1018582423406
14. Haneda K., Miyakawa C., Kojima H. (1974): Preparation of High-Coercivity $BaFe_{12}O_{19}$. *Journal of the American Ceramic Society*, *57*(8), 354-357. doi: 10.1111/j.1151-2916.1974.tb10921.x
15. Ataie A., Piramoo, M.R., Harris I.R., Ponton C.B. (1995): Effect of hydrothermal synthesis environment on the particle morphology, chemistry and magnetic properties of barium hexaferrite. *Journal of materials science*, *30*(22), 5600-5606. doi: 10.1007/BF00356692
16. Kumazawa H., Maeda Y., Sada E. (1995): Further consideration of hydrothermal synthesis of barium ferrite fine particles. *Journal of materials science letters*, *14*(1), 68-70. doi: 10.1007/BF02565290
17. Pillai V., Kumar P., Shah D.O. (1992): Magnetic properties of barium ferrite synthesized using a microemulsion mediated process. *Journal of magnetism and magnetic materials*, *116*(3), L299-L304. doi:10.1016/0304-8853(92)90105-W
18. Irfan M., Islam M.U., Ali I., Iqbal M.A., Karamat N., Khan H.M. (2014): Effect of Y_2O_3 doping on the electrical transport properties of $Sr_2MnNiFe_{12}O_{22}$ Y-type hexaferrite. *Current Applied Physics*, *14*(1), 112-117. doi:10.1016/j.cap.2013.10.010
19. Rezlescu N., Rezlescu E., Pop, P. D., Rezlescu L. (1998) : Effects of rare-earth oxides on physical properties of Li–Zn ferrite. *Journal of alloys and compounds*, *275*, 657-659. doi:10.1016/S0925-8388(98)00413-7
20. McCrum N.G., Read B.E., Williams G. (1967). *Anelastic and Dielectric Effects in Polymeric Solids*, Wiley, New York.
21. Chowdari B.V.R., Gopalakrishnan R. (1987): AC conductivity analysis of glassy silver iodomolybdate system. *Solid State Ionics*, *23*(3), 225-233. doi: 10.1016/0167-2738(87)90055-5
22. Costa M.M., Pires Junior G.F.M., Sombra A.S.B. (2010): Dielectric and impedance properties' studies of the of lead doped (PbO)-Co_2Y type hexaferrite ($Ba_2Co_2Fe_{12}O_{22}$ (Co_2Y)). *Materials Chemistry and Physics*, *123*(1), 35-39. doi: 10.1016/j.matchemphys.2010.03.026
23. Patange S.M., Shirsath S.E., Lohar K.S., Jadhav S.S., Kulkarni N., Jadhav K.M. (2011): Electrical and switching properties of $NiAl_xFe_{2-x}O_4$ ferrites synthesized by chemical method. *Physica B: Condensed Matter*, *406*(3), 663-668. doi: 10.1016/j.physb.2010.11.081
24. Rodrigues H.O., Pires Junior G.F.M., Sales A.J.M., Silva P.M.O., Costa B.F.O., Alcantara Jr. P., Moreira S.G.C., Sombra A.S.B. (2011): $BiFeO_3$ ceramic matrix with Bi_2O_3 or PbO added: Mössbauer, Raman and dielectric spectroscopy studies. *Physica B: Condensed Matter*, *406*(13), 2532-2539. doi: 10.1016/j.physb.2011.03.050
25. Irfan M., Niaz N.A., Ali I., Nasir S.,Shakoor A., Aziz A., Karamat N., Khalid N.R. (2015): Dielectric Behavior and Magnetic Properties of Mn-Substituted Ni–Zn Ferrites, *Journal of Electronic Materials*, doi: 10.1007/s11664-015-3770-0
26. Bai Y., Zhou J., Gui Z., Li L. (2004) : Electrical properties of non-stoichiometric Y-type hexagonal ferrite. *Journal of magnetism and magnetic materials*, *278*(1), 208-213. doi: 10.1016/j.jmmm.2003.12.1389
27. Chourashiya M.G., Patil J.Y., Pawar S.H., Jadhav L.D. (2008): Studies on structural, morphological and electrical properties of $Ce_{1-x}Gd_xO_{2-(x/2)}$. *Materials Chemistry and Physics*, *109*(1), 39-44. doi:10.1016/j.matchemphys.2007.10.028
28. Skomski R., Coey J.M.D. (1999). *Permanent magnetism*, British Library Cataloguing-in-Publication data, ISBN 0750304782.
29. Ali I., Islam M.U., Awan M.S., Ahmad M., Ashiq M.N., Naseem S. (2013): Effect of Tb^{3+} substitution on the structural and magnetic properties of M-type hexaferrites synthesized by sol–gel auto-combustion technique. *Journal of Alloys and Compounds*, *550*, 564-572.
30. Thongmee S., Winotai P., Tang I.M. (2003): Boron site preference in B-doped barium hexaferrite. *Science Asia*, *29*, 51-55.
31. Elahi A., Ahmad M., Ali I., Rana, M.U. (2013): Preparation and properties of sol–gel synthesized Mg-substituted Ni_2Y hexagonal ferrites. *Ceramics International*, *39*(2), 983-990. doi: 10.1016/j.ceramint.2012.07.016
32. Al-Omari I.A., Skomski R., Sellmyer D.J. (2012): Magnetic roperties of $Y_{3-2x}Ca_{2x}Fe_{5-x}V_xO_{12}$ Garnets. *Advances in Materials Physics and Chemistry*, *2*, 116-120. doi: 10.4236/ampc.2012.23019
33. Ali I., Islam M.U., Ishaque M., Khan H.M., Ashiq M.N., Rana M.U. (2012): Structural and magnetic properties of holmium substituted cobalt ferrites synthesized by chemical co-precipitation method. *Journal of Magnetism and Magnetic Materials, 324*(22), 3773-3777. doi: 10.1016/j.jmmm.2012.06.008
34. Shirsath S.E., Toksha B.G., Jadhav K.M. (2009): Structural and magnetic properties of In^{3+} substituted $NiFe_2O_4$. *Materials Chemistry and Physics, 117*(1), 163-168. doi:10.1016/j.matchemphys.2009.05.027
35. Lechevallier L., Le Breton J.M., Morel A., Teillet J. (2003): Structural and magnetic properties of $Sr_{1-x}Sm_xFe_{12}O_{19}$ hexagonal ferrites synthesised by a ceramic process. *Journal of alloys and compounds, 359*(1), 310-314. doi:10.1016/S0925-8388(03)00206-8
36. Ahmed M.A., Okasha N., Kershi R. M. (2008): Influence of rare-earth ions on the structure and magnetic properties of barium W-type hexaferrite. *Journal of Magnetism and Magnetic Materials*, *320*(6), 1146-1150. doi:10.1016/j.jmmm.2007.11.014
37. Bammannavar B.K., Naik L.R., Pujar R.B., Chougule B.K. (2007): Preparation, characterization and physical properties of Mg–Zn ferrites. *Indian Journal of Engineering and Materials Sciences*, *14*(5), 381.
38. Panneer Muthuselvam I., Bhowmik, R. N. (2010): Mechanical alloyed Ho^{3+} doping in $CoFe_2O_4$ spinel ferrite and understanding of magnetic nano domains. *Journal of Magnetism and Magnetic Material*s, *322*(7), 767-776. doi:10.1016/j.jmmm.2009.10.057
39. Rashad M.M., Mohamed, R.M., El-Shall H. (2008): Magnetic properties of nanocrystalline Sm-substituted $CoFe_2O_4$ synthesized by citrate precursor method. *Journal of Materials Processing Technology*, *198*(1), 139-146. doi: 10.1016/j.jmatprotec.2007.07.012